Data-Aided Collaborative Planning of Energy Storage for Remote Renewable Base

Weile Kong [a], Hongxing Ye [a,*], Yinyin Ge[a], Zhidong Wang[b], Yi Huang[b], Zhi An[b]

[a] *Xi'an Jiaotong University, Xi'an, 710049, Shaanxi, China*
[b] *State Grid Economic and Technological Research Institute, Beijing, 102209, China*

Abstract

Renewable bases are typically located far from load centers. High-voltage direct current tie-lines have therefore emerged as a promising solution for transmitting remote renewable power to load centers. Effective planning of energy storage and tie-line transmission power in inter-regional systems is crucial for promoting large-scale renewable accommodation. This work proposes a data-aided planning framework for inter-regional power systems that incorporates bidirectional flexibility from both energy storage and thermal units. A temporally correlated interval prediction method is developed to construct a data-informed operational envelope. By explicitly capturing temporal correlations in prediction errors, the resulting uncertainty intervals are tightened, thereby reducing planning conservatism. Flexibility-sharing and deliverability constraints are integrated into the framework to ensure operational robustness while lowering overall investment costs. The proposed data-aided planning framework enables flexibility deployed in the planning stage to accommodate operational uncertainties. To handle nonlinear terms arising from deep peak-regulation constraints of thermal units, a piecewise least-squares linearization technique is introduced, transforming the problem into a mixed-integer linear programming formulation. Simulation results indicate that bidirectional flexibility reduces investment and operational costs. Comparable robustness is attained under less conservative flexibility constraints, which further contributes to cost savings. The proposed linearization approach solves the problem effectively while maintaining acceptable optimality.

Keywords: Energy storage, bidirectional flexibility, prediction interval, piecewise least-square linearization, remote renewable base

Nomenclature

Indices

e	index of storage
g	index of thermal units
t	index of time intervals

Parameters

α	confidence level
Δt	time resolution
$\eta^{A,c}, \eta^{A,d}$	charge/discharge efficiency
$\overline{\epsilon}^{r,nl}_{t,\alpha}, \underline{\epsilon}^{r,nl}_{t,\alpha}$	upper/lower bounds of uncertainty at receiving end with confidence level α
$\overline{\epsilon}^{s,nl}_{t,\alpha}, \underline{\epsilon}^{s,nl}_{t,\alpha}$	upper/lower bounds of uncertainty at sending end with confidence level α
c^{inv}_e, c^{inv}_p	unit investment cost of storage energy capacity and power capacity
c^{rec}_e	unit recycle cost of the remaining storage energy capacity
c^o_g	cost of the unit generation
d_g, e_g	coefficients of oil consumption cost
$L^{A,f}_t$	forecast load demand at t
L^A_t	load demand at t
M	a big positive value
N^A_g	unit number at A end
P^{wf}_t, P^{pvf}_t	forecast wind/photovoltaic power at t
Q^{dc}	Contracted trading electricity
S_g	unit investment cost
S^{oil}_g	unit oil consumption cost during oil injection regulation
$P^A_{g,a}, P^A_{g,b}$	min output of unit g during deep peak regulation and oil injection regulation
$P^A_{g,min}, P^A_{g,max}$	min/max output of unit g
$P^{dc}_{min}, P^{dc}_{max}$	transmission capacity of tie-line
$R^{dc,up}, R^{dc,dn}$	admitted upward/downward adjustment amplitude of tie-line power
$R^{A,up}_g, R^{A,dn}_g$	upward/downward ramp rate of unit g

Variables

E^A_0, E^A_T	energy level at first/last time slot
E^{real}_t	real capacity of storage with aging
E^A_{max}, E^A_{min}	max/min energy level of storage
E^A_t	energy level of storage at t
n^A	the number of deployed storage
$P^A_{g,t}$	output of thermal unit g at t
$P^{A,c}_{max}, P^{A,d}_{max}$	max storage charge/discharge power
$P^{A,c}_t, P^{A,d}_t$	storage charge/discharge power at t
$u^{A,c}_t, u^{A,d}_t$	charge/discharge status of storage at t
P^{dc}_t	transmission power of tie-line at t
$r^{A,up}_{g,t}, r^{A,dn}_{g,t}$	unit upward/downward reserve at t
$r^{A,e,up}_t, r^{A,e,dn}_t$	storage upward/downward reserve at t
$r^{dc,+}_t, r^{dc,-}_t$	upward/downward adjustable power of tie-line at t
$r^{r-s,up}_t, r^{r-s,dn}_t$	upward/downward reserve shared from receiving end at t
$r^{s-r,up}_t, r^{s-r,dn}_t$	upward/downward reserve shared from sending end at t

1. Introduction

Driven by global environmental policies, renewable energy sources have experienced rapid growth in recent years. Due to geographical features, utility-scale wind and photovoltaic (PV) generation bases are typically located far from load centers. High voltage direct current (HVDC) technology offers significant advantages in bulk power transmission and inter-regional energy support

*Corresponding author
Email address: yehxing@xjtu.edu.cn (Hongxing Ye)

[1]. Compared to high-voltage alternating current (HVAC), HVDC offers lower capital and operating costs, reduced power losses, and a smaller physical footprint. It enables stable long-distance power transfer without the need for reactive power compensation, facilitates the interconnection of asynchronous grids, and enhances overall system stability through more flexible control. According to data released on the official website of the Chinese government, China had completed and commissioned 42 ultra-high-voltage alternating-current and direct-current transmission projects by the end of 2024 [2]. Among these projects, 20 are HVDC and 22 are HVAC, together providing a cross-provincial and cross-regional transmission capacity exceeding 300 GW. Furthermore, as reported by China Central Television, by late November 2025, the number of operational ultra-high-voltage transmission lines had increased to 44 [3]. In addition, HVDC projects have been widely deployed worldwide to transmit renewable electricity to geographically dispersed load centers [4]. In recent years, many remote renewable bases (RRBs) have been developed, providing both economic and environmental benefits [5]. However, the inherent volatility and uncertainty of renewable energy sources pose significant challenges in the planning and operation of transmission systems when integrating a large share of renewable energy [6]. In highly renewable scenarios, the strategic deployment of flexible resources, such as energy storage, is essential for the reliable and cost-effective operation of inter-regional power systems in medium- to long-term planning.

Taking advantage of the complementary characteristics of inter-regional resources, a strategic tie-line transmission plan can improve the accommodation of remote renewable energy [7]. There is a rich literature focusing on operational economics in the context of remote renewable accommodation. It is effective to jointly optimize the inter-regional resources and predetermine the tie-line transmission plan [8]. However, uncertainty is not considered, which may lead to infeasible scenarios during real-time operation. To address renewable uncertainty, different robust models and methods for inter-regional systems are established to improve economic performance and ensure operational robustness [9, 10]. Most of the above-mentioned works overlook the flexibility-sharing capability of the tie-line, which could further improve operational economics.

Tie-lines can be strategically scheduled to maximize flexibility sharing and accommodate the uncertainty of RRB, which expands the feasible operating region of the power system [11]. The secure operation region of HVDC is quantified in [12] to maximize the utilization of renewable en-

ergy. Some studies have focused on the shareable reserve between interconnected regions, which can enhance both system reliability and economic efficiency [13, 14]. To ensure that flexibility can be delivered to required locations, deliverability should be incorporated [15–17]. However, the above-mentioned researches are mainly focused on the real-time operational level. There exists a research gap in developing a planning framework for inter-regional power systems that explicitly embeds operational robustness and flexibility constraints.

Reliability and economic efficiency in inter-regional power system planning have also drawn considerable research interest. Many existing works have focused on the planning of flexible resources. Coordinated expansion planning of HVDC/HVAC transmission lines can improve reliability and reduce costs in inter-regional power systems [18]. In addition, flexible resources deployed at the planning stage are also significant, as they can accommodate operational uncertainty. Deep peak regulation of thermal units can reduce dual peak-shaving pressure and promote renewable accommodation in HVDC systems [19]. However, the nonlinear characteristic introduced by variable operating conditions is often overlooked, causing an intractable problem. Efficient modeling of variable operating conditions of deep peak regulation units remains largely unexplored in the existing literature. Various types of storage are deployed to promote the accommodation of inter-regional renewable generation [20, 21]. The co-planning of energy storage and tie-line power is utilized to alleviate transmission congestion and increase renewable accommodation. These works typically formulate uncertainty using budget sets [9, 10, 20] or stochastic scenarios [21] derived from empirical distributions, which may not fully reflect actual renewable generation patterns. In addition, overly conservative reserve provision strategies result in redundant investments. Therefore, the degree of conservatism in reserve provision should be further analyzed to tradeoff system robustness and investment cost. This motivates further exploration of a planning framework with an embedded operational uncertainty envelope to quantify flexibility requirements and ensure the robustness of planning outcomes.

Based on a review of the existing literature, the identified gaps are summarized in Table 1. However, there are still some unresolved challenges in the planning and operation of the inter-regional power system. With the increasing availability of operational data, data-driven approaches offer a promising way for systems planning and scheduling [22]. To leverage valuable historical

Table 1: Comparison of the proposed work with representative existing studies

Ref.	Planning / Operation	Uncertainty Modeling	Temporal Correlation	HVDC-Based Flexibility	Deliverable Reserve Sharing	PI Quality Metrics	Storage Sizing
[8]	Operation	Deterministic	×	✓	×	×	×
[9]	Operation	Robust	×	✓	×	×	×
[10]	Operation	Robust	×	✓	×	×	×
[11]	Operation	Scenario-based	×	✓	×	×	×
[12]	Planning	Deterministic	×	✓	×	×	×
[13]	Operation	Robust	×	✓	×	×	×
[14]	Operation	Scenario-based	×	✓	×	×	×
[15]	Operation	Stochastic	✓	×	✓	×	×
[16]	Operation	Dist.-robust	×	×	×	×	×
[17]	Operation	Deterministic	×	×	✓	×	×
[18]	Planning	Scenario-based	×	✓	×	×	×
[19]	Operation	Deterministic	×	✓	×	×	×
[20]	Planning	Scenario-based	×	✓	×	×	×
[21]	Planning	Probabilistic	×	✓	×	×	✓
[22]	Operation	Prediction Interval (PI)	×	×	×	✓	×
This work	**Planning + Operation**	**PI**	✓	✓	✓	✓	✓

data and address identified research gaps, this work presents a data-aided planning framework for inter-regional power systems. It incorporates deliverability and conservatism constraints on flexibility, along with a piecewise least-squares linearization technique, to ensure both efficiency and effectiveness. A temporally correlated prediction interval is constructed to represent the data-informed operational envelope of net load, thereby ensuring operational robustness. The main contributions of this paper are summarized as follows.

- A novel data-aided planning framework incorporating operational constraints is proposed to ensure operational robustness for inter-regional power systems. Existing uncertainty modeling typically accounts for time-independent uncertainty sets [10, 20, 21]. However, renewable generation deviations tend to exhibit temporal correlation over consecutive periods under persistent weather conditions. The proposed model aims to construct a temporally correlated prediction interval that quantifies the operational uncertainty envelope.

- A data-informed approach is proposed to reduce storage investment costs while maintaining robustness. As net load uncertainty rarely remains persistently positive or negative within successive periods, adopting an overly conservative strategy for storage deployment is often unnecessary. There is an emerging research need for the strategic planning of flexible

resources. The proposed data-informed approach achieves an effective tradeoff between investment costs and system robustness.

- A piecewise least-squares linearization method is proposed to address the nonlinearity in variable operating conditions of unit deep peak regulation. By approximating the nonlinear terms, the optimization problem is recast as a Mixed-Integer Linear Program (MILP), which can be efficiently solved using off-the-shelf solvers.

The remainder of this paper is organized as follows. Section II provides an overview of the data-aided planning framework and the temporally correlated prediction interval. Section III presents the proposed planning framework, including embedded operational constraints and the piecewise least-squares linearization method. Case studies are conducted in Section IV. Section V concludes the paper.

2. Problem Description

In this section, we propose the planning framework and the data-aided uncertainty interval prediction method. The base net load is estimated by the gate recurrent unit (GRU) network. The operational envelope is quantified by the conditional kernel density estimation (KDE), which captures the temporal correlation of prediction errors. The framework incorporates flexibility, deliverability, and conservatism, along with piecewise least-squares linearization, to ensure both operational robustness and computational efficiency. The coordination among these components is illustrated in Fig. 1.

2.1. Decision Framework

The proposed planning framework, which incorporates operational constraints, is formulated as an optimization problem with both long-term and short-term decision variables. The multi-timescale decision framework is illustrated in Fig. 2. From a long-term perspective, the planner aims to minimize the investment cost of battery storage. In short-term operation, the operator schedules sufficient flexibility to ensure operational robustness. The planning model aims to minimize the expected operational cost over a planning horizon of Y years.

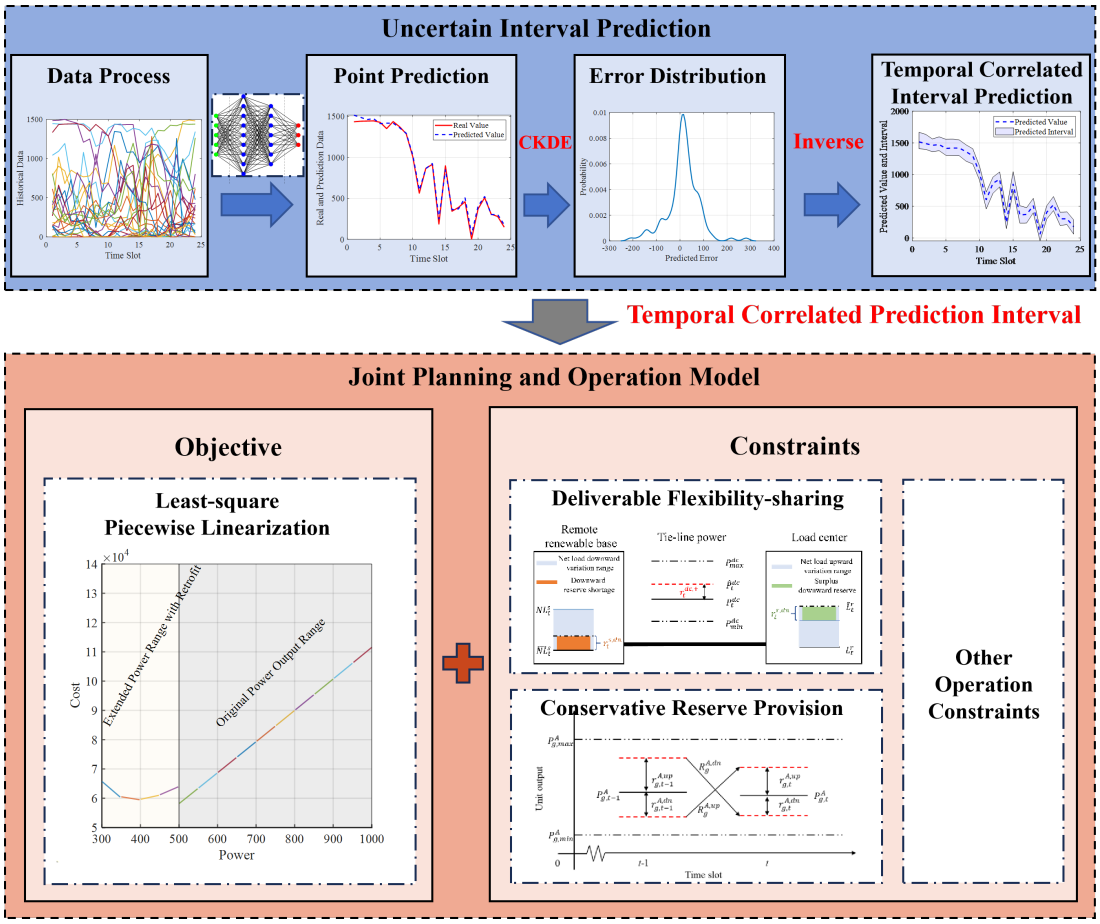

Fig. 1. The diagram of the proposed data-aided planning framework with operational constraints.

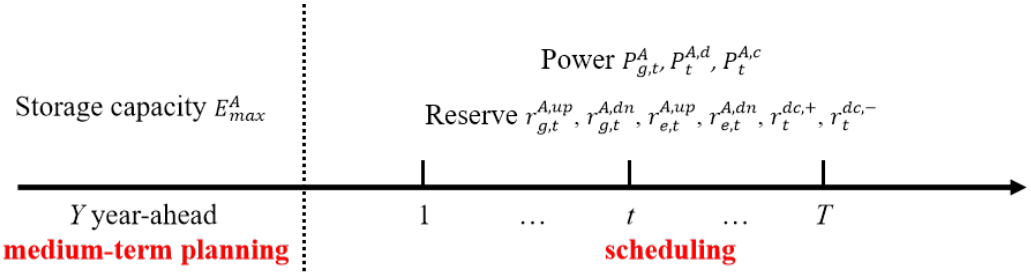

Fig. 2. Framework of planning and operation decisions.

The planning model employs a representative day approach with an hourly resolution. To capture seasonal variations while maintaining computational tractability, one typical day is selected for each season, resulting in four 24-hour scenarios that form the basis of the operational simulation within the planning horizon. These typical days are derived from clustering historical data for each season.

In the inter-regional grid, it is assumed that the planner has access to historical data on renewable generation and load. Base scenarios and prediction intervals are derived from seasonal data. In the planning stage, optimal storage capacities are determined. To ensure operational robustness, sufficient flexibility must be reserved to maintain balance during the operational stage.

2.2. Uncertainty Interval Prediction

To ensure operational robustness, uncertainties in load and renewable generation must be considered when optimally deploying flexible resources. In the literature, normal and truncated normal distributions are commonly used to model forecast errors. However, such assumed distributions may not accurately reflect real-world forecast errors [23]. Uncertainty intervals are usually used in robust planning and operation of power systems [22, 24]. Given the time-dependent forecast errors, a temporally correlated prediction interval is proposed based on a nonparametric conditional KDE method. Because the prediction interval is constructed for flexibility-oriented planning, the model assumes stationarity within the considered operational scenarios and does not explicitly account for non-stationarity or regime shifts. The uncertainty interval prediction process is presented below.

- **Data Processing:** Due to the sensitivity of deep learning-based prediction models to data scale, historical data for weather P and renewable/load X are normalized to the range [0,1] using eq. (1). The datasets are then categorized into training and testing sets.

$$\phi_{scale} = \frac{\phi - \phi_{min}}{\phi_{max} - \phi_{min}} \tag{1}$$

- **Point Prediction:** Scaled weather P_{scale} and renewable/load X_{scale} series are incorporated as input data. The point prediction model is implemented using a GRU network, as shown in Fig.3. Here, Y represents the output vector of the predicted values. The learning process minimizes the difference between the predicted and actual values. Then, renewable generation and load are obtained using the trained model with weather features.

- **Distribution of Prediction Errors:** Based on the training data sample $\{(p_i, x_i)|i \in \{1, 2, \cdots, n\}\}$, the estimated values of x_i are calculated via the GRU network as y_i. The prediction errors ϵ

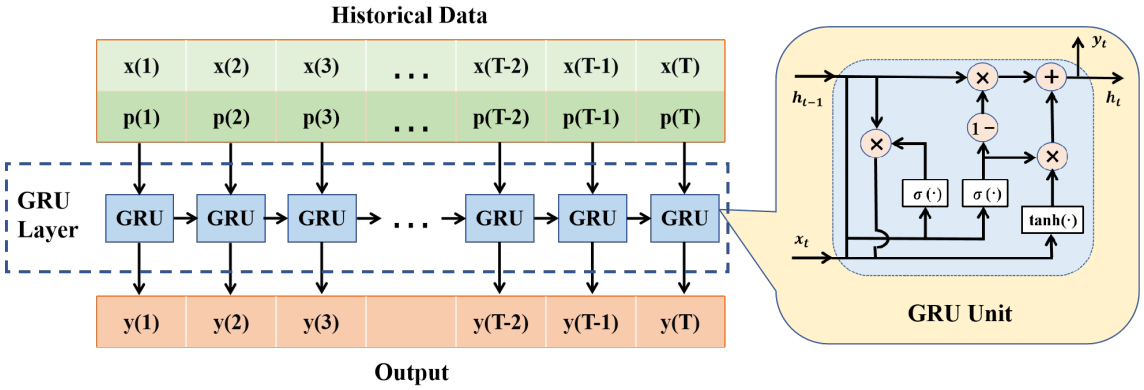

Fig. 3. The structure of the GRU model.

are then calculated as the difference between observed and predicted values, $\epsilon_i = y_i - x_i,\ i = 1, 2, \ldots, n$.

The temporal correlation of forecast errors allows for tighter uncertainty quantification, leading to more realistic flexibility requirements [25, 26]. Here, conditional KDE is applied to estimate the time-dependent uncertainty intervals. The conditional density is estimated by (2), where K_h denotes the Gaussian kernel function.

$$\hat{f}_{\Xi_{\tau^*}|\Xi_{\tau^*-k:\tau^*-1},Y_{\tau^*}}(\epsilon \mid \epsilon_{\tau^*-k:\tau^*-1}, y^*_{\tau^*}) = \frac{\sum_{i=1}^{n} K_h(y^*_{\tau^*} - y_{i,\tau^*}) K_h(\epsilon - \epsilon_{i,\tau^*}) \prod_{j=1}^{k} K_h(\epsilon^*_{\tau^*-j} - \epsilon_{i,\tau^*-j})}{\sum_{i=1}^{n} K_h(y^*_{\tau^*} - y_{i,\tau^*}) \prod_{j=1}^{k} K_h(\epsilon^*_{\tau^*-j} - \epsilon_{i,\tau^*-j})} \tag{2}$$

Integrating $\hat{f}_{\Xi_{\tau^*}|\Xi_{\tau^*-k:\tau^*-1},Y_{\tau^*}}(\epsilon \mid \epsilon_{\tau^*-k:\tau^*-1}, y^*_{\tau^*})$, the cumulative distribution function is obtained by (3).

$$\hat{F}_{\Xi_{\tau^*}|\Xi_{\tau^*-k:\tau^*-1},Y_{\tau^*}}(\epsilon \mid \epsilon_{\tau^*-k:\tau^*-1}, y^*_{\tau^*}) = \int_{-\infty}^{\epsilon} \hat{f}_{\Xi_{\tau^*}|\Xi_{\tau^*-k:\tau^*-1},Y_{\tau^*}}(u \mid \epsilon_{\tau^*-k:\tau^*-1}, y^*_{\tau^*})\, du \tag{3}$$

- **Interval Prediction:** Given a confidence level β, the prediction interval for the target time step is constructed using the conditional cumulative distribution function of the forecast error $\hat{F}_{\Xi_{\tau^*}|\Xi_{\tau^*-k:\tau^*-1},Y_{\tau^*}}(\epsilon \mid \epsilon_{\tau^*-k:\tau^*-1}, y^*_{\tau^*})$. The lower and upper bounds of the prediction errors

are defined as the quantiles of this conditional distribution, given in (4) and (5), respectively.

$$\underline{\epsilon}^{A,nl}_{\tau^*,\alpha} = \hat{F}^{-1}_{\Xi_{\tau^*}|\mathbf{\Xi}_{\tau^*-k:\tau^*-1},Y_{\tau^*}}\Big(\frac{1-\alpha}{2}\Big) \tag{4}$$

$$\overline{\epsilon}^{A,nl}_{\tau^*,\alpha} = \hat{F}^{-1}_{\Xi_{\tau^*}|\mathbf{\Xi}_{\tau^*-k:\tau^*-1},Y_{\tau^*}}\Big(1-\frac{1-\alpha}{2}\Big) \tag{5}$$

Finally, the prediction interval U^{pi} is obtained by adding the upper and lower bounds to the prediction values, as $U^{pi} = \{y^*_{\tau^*} + \underline{\epsilon}^{A,nl}_{\tau^*,\alpha} \leq \hat{y} \leq y^*_{\tau^*} + \overline{\epsilon}^{A,nl}_{\tau^*,\alpha}\}$.

It is noted that the forecast error distribution estimated by our conditional KDE model encapsulates a blend of epistemic and aleatory uncertainties. For robust flexibility planning, we treat this composite distribution as a practical representation of the total operational uncertainty that the system must be prepared to handle.

3. Model Formulation

This section formulates the planning model for an inter-regional power system with embedded operational constraints. First, the total investment and operation objective is established. Then, the linearization technique is proposed to approximate the nonlinear terms in the objective. Finally, a solvable planning model is formulated.

3.1. Model Objective

The objective is to minimize the total investment and operational cost over Y years. The equivalent annual annuity method, as used in [27], is applied to calculate the cost. Storage capacities are determined in the planning stage. During the operation stage, flexibility is allocated to manage uncertainties in renewable generation and load. The objective function is formulated in Eq.(6). The first term represents the storage investment cost. The second term represents the unit operational cost.

$$\min \boldsymbol{f}^{obj} = \frac{\gamma(1+\gamma)^Y}{(1+\gamma)^Y-1}\sum_{A\in\{s,r\}}\Big\{c^{inv}_e E^A_{max} + c^{inv}_p P^{A,c}_{max} - c^{rec}_e E^A_T\Big\} + \sum_{A\in\{s,r\}}\sum_{t\in\mathcal{Y}}\sum_{g=1}^{Ng} c^o_g(P^A_{g,t}) \tag{6}$$

The superscript $A \in \{s, r\}$ represents that the variable is associated with the sending end s or the receiving end r. $c_g^o(P_{g,t}^A)$ represents the operational cost of the thermal unit.

3.1.1. Thermal Unit Operational Cost

Deep peak regulation of the unit leads to variable operational conditions. Due to deep peak regulation, the unit operating below a certain power threshold incurs additional costs, including fuel, fatigue, and oil injection costs. Thus, the unit operation cost is modeled as a piecewise function in (7).

$$c_g^o(P_{g,t}^A) = \begin{cases} (aP_{g,t}^{A^2} + bP_{g,t}^A + c), & P_{g,min}^A \le P_{g,t}^A \le P_{g,max}^A \\ (2 - \dfrac{P_{g,t}^A}{P_{g,min}^A}) \cdot (aP_{g,t}^{A^2} + bP_{g,t}^A + c) + \dfrac{\beta S_g}{2N_t(P_{g,t}^A)}, & P_{g,a}^A \le P_{g,t}^A \le P_{g,min}^A \\ (2 - \dfrac{P_{g,t}^A}{P_{g,min}^A}) \cdot (aP_{g,t}^{A^2} + bP_{g,t}^A + c) + \dfrac{\beta S_g}{2N_t(P_{g,t}^A)} + S_g^{oil} \cdot (d_g P_{g,t}^A + e_g), & P_{g,b}^A \le P_{g,t}^A \le P_{g,a}^A \end{cases} \tag{7}$$

in which $(aP_{g,t}^{A^2} + bP_{g,t}^A + c)$ represents the fuel cost in regular operation, while $(1 - P_{g,t}^A / P_{g,min}^A) \cdot (aP_{g,t}^{A^2} + bP_{g,t}^A + c)$ represents the additional coal cost during the peak regulation stage [28]. The second term in the second row is the fatigue cost. The third term in the third row is the oil injection cost. According to [29], it is formulated as a linear function of the generation output. $N_t(P_{g,t}^A)$ denotes the number of cracking cycles of the rotor. Referring to [30, 31], the fatigue cost can be described using the Manson–Coffin equation. It is noted that fitting approaches can be applied to approximate the unit fatigue cost [32, 33]. The schematic diagram of the unit's piecewise nonlinear cost function is shown in Fig.4.

3.1.2. Storage Investment and Operational Cost

Battery storage investment and operational costs are incorporated into the planning problem. The investment cost includes capital expenditures for both the energy and power capacity ratings. In addition, battery storage systems degrade over time, reducing their available capacity and operational performance. Consequently, degradation costs [34], comprising components of calendar

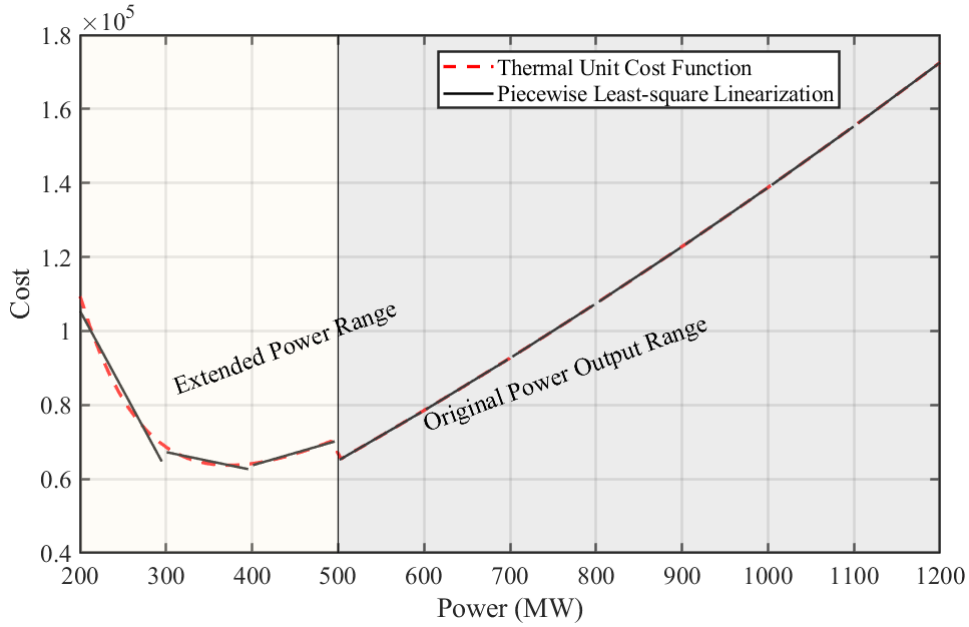

Fig. 4. Schematic diagram of a piecewise function of unit deep peak regulation.

aging and cycle aging, are integrated into the planning model.

$$\Lambda_t^{A,cal} = \left[\left(\frac{t}{720}\right)^{0.8} - \left(\frac{t-1}{720}\right)^{0.8}\right](\beta_1 S_t^A + \beta_2 E_t^A) \tag{8}$$

$$\Lambda_t^{A,cyc} = (\Lambda_t^{A,temp} - \Lambda_{t-1}^{A,temp}) \cdot u_t^{A,d} \tag{9}$$

$$\sum_{m=1}^{N^m} v_{t,m}^A \le 1 \tag{10}$$

$$0 \le S_{t,m}^A \le D_m \cdot v_{t,m}^A \tag{11}$$

$$S_{min}^A + \sum_{m=1}^{N^m} \left[S_{t,m}^A + D_m \cdot (m-1) \cdot v_{t,m}^A\right] = S_t^A \tag{12}$$

$$\Lambda_t^{A,temp} = \sum_{m=1}^{N^m} \left[\gamma_m^A \cdot S_{t,m}^A + N^A(S_M^{ini}) \cdot v_{t,m}^A\right] \tag{13}$$

in which $\Lambda_t^{A,cal}$ and $\Lambda_t^{A,cyc}$ are the calendar and the cycling aging at time t. $\Lambda_t^{A,temp}$ is the decline in capacity caused by the charging and discharging process. E_t^A and S_t^A represent the actual capacity and state of charge (SOC) of storage at time t. S_{min}^A is the minimum allowable SOC. $S_{t,m}^A$ is the SOC in segment m at time t. $v_{t,m}^A$ is the binary indicator for segment selection. D_m is the length of

the segment m. N^m is the total number of segments. γ_m^A is the slope of segment m. $N^A(S_M^{ini})$ is the faded capacity under SOC S_M^{ini}.

Eq. (8) is a linear form of calendar aging. Eq. (9) is the calculation of cycling aging. Constraints (10)-(13) are the piecewise linear approximation of the cycle life function. Constraint (10) ensures that only one segment can be selected. Constraint (11) limits the SOC within each segment. Eq.(12) ensures that the linearized SOC equals the actual one. Eq.(13) defines the amount of capacity fading within each charge or discharge process.

3.2. Piecewise Least-square Linearization

The nonlinear terms associated with deep peak regulation cause computational difficulty. Piecewise linear approximation methods are usually used to deal with nonlinear functions. In this work, we propose a piecewise least-squares linearization technique to approximate the cost function based on the sampled points on the nonlinear curve. The function is divided into l segments, each fitted by the least-squares linear approximation. The criterion is to minimize the difference between the nonlinear function and its linear approximation, as expressed in (14).

$$\min \sum_{i=1}^{N_l} (k_l x_{l,i} + h_l - y_{l,i})^2 \tag{14}$$

where k_l and h_l are the slope and intercept of the lth linear segment to be optimized. $x_{l,i}$ represents the ith sample in the lth segment. $y_{l,i}$ is the value of the nonlinear function associated with $x_{l,i}$. The pair $(x_{l,i}, y_{l,i})$ is used to determine the slope and the intercept. In this work, $x_{l,i}$ is the unit output sample related to $P_{g,t}^A$ and $y_{l,i}$ is the corresponding operating cost $c_g^o(P_{g,t}^A)$. The points are sampled uniformly within the relevant operating ranges. Specifically, the break points of the discontinuous function are selected as the boundaries of the fragmented segments.

For simplicity, the optimization problem for each segment with n sampled data points is rewritten in the following matrix form. C is the coefficient matrix. I is a vector of ones. X is the vector of the sampled unit output. Y is the vector of the sampled unit generation costs.

$$\min ([I^T, X^T] \cdot C - Y)^T \cdot ([I^T, X^T] \cdot C - Y) \tag{15}$$

$$s.t.\ C = (K_l, H_l)^T \tag{16}$$

$$I = (1, 1, \ldots, 1) \tag{17}$$

$$X = (x_{l,1}, x_{l,2}, \ldots, x_{l,n}) \tag{18}$$

$$Y = (y_{l,1}, y_{l,2}, \ldots, y_{l,n}) \tag{19}$$

By substituting coefficient matrices (16)-(17) and variable matrices (18)-(19) in the least-squares objective (15), the optimization problem to minimize the least-squares error is inherently an unconstrained program. Then, the optimal coefficients C^* can be derived based on stationary point theory, as $C^* = ([I^T, X^T] \cdot [I^T, X^T]^T)^{-1} \cdot X \cdot Y$. Once the slope and intercept coefficients are obtained, the approximated function for each linear segment is given by $\hat{Y} = [I^T, \hat{X}^T] \cdot C^*$.

Finally, the nonlinear terms associated with deep peak regulation of thermal units are linearized via piecewise linear segments, as illustrated in Fig. 4. Applying a special order set constraint of type 2, the linear segments can be transformed into a set of mixed-integer linear constraints. Let π_l denote the partition points of the segments. Continuous auxiliary variables $\omega_l \geq 0$ and binary variables $s_l \in \{0, 1\}$ are introduced to formulate piecewise linear functions as $\hat{c}(\cdot)$.

$$\hat{c}(x) = \sum_{l=1}^{L+1} \omega_l \cdot (k_l \pi_l + h_l), \quad x = \sum_{l=1}^{L+1} \omega_l \pi_l \tag{20}$$

$$\omega_1 \leq s_1, \quad \omega_L + 1 \leq s_L, \quad \omega_l \leq s_{l-1} + s_l, \quad \sum_{l=1}^{L+1} \omega_l = 1, \quad \sum_{l=1}^{L} s_l = 1 \tag{21}$$

Then, the objective is converted into a mixed-integer linear formulation.

3.3. Planning Model

Sufficient flexible resources are essential in the planning stage to address operational uncertainties. Operational constraints are embedded in the planning framework to ensure robustness in the operation stage. Then, a chance-constrained programming model is established to ensure that the reserve can accommodate uncertainties within the prediction interval.

3.3.1. Power Balance Equation

The inter-regional power balance should be maintained within each end. Eqs. (22) and (23) represent the power balance at the sending and receiving ends, respectively. Equation (24) represents the network constraints that ensure the availability of reserves.

$$\sum\nolimits_{g\in\mathcal{G}^s} P^s_{g,t} + P^{wf}_t + P^{pvf}_t - P^{s,c}_t + P^{s,d}_t - P^{dc}_t = L^{s,f}_t \tag{22}$$

$$\sum\nolimits_{g\in\mathcal{G}^r} P^r_{g,t} + P^{dc}_t - P^{r,c}_t + P^{r,d}_t = L^{r,f}_t \tag{23}$$

$$-F^A_l \le \sum_i \Gamma^A_{l,i}\Big(\sum_{g\in\mathcal{S}^{g,A}_{(i)}}(P^A_{g,t}+\Delta P^A_{g,t}) + \sum_{e\in\mathcal{S}^{e,A}_{(i)}}(P^{A,d}_t - P^{A,c}_t + \Delta P^{A,e}_t) - (L^{A,f}_{i,t}+\epsilon^A_{i,t})\Big) \le F^A_l \tag{24}$$

In which $\Gamma^A_{l,i}$ is the power transfer distribution factor matrix for nodal power injection. F^A_l represents the transmission capacity. $\Delta P^A_{g,t}$ is the generation reserve. $\epsilon_{i,t}$ is the net load deviation of node i at time t.

3.3.2. Thermal Unit Constraints

Deep peak regulation is considered for thermal units to boost their flexibility. Constraints (25) and (26) limit the output range of thermal units under regular operation, deep peak regulation, or oil injection regulation status. Eq. (27) ensures that each unit can have only one operational status at any given t. Constraints (28) and (29) limit the ramping capacity of the thermal units. Constraints (30)-(33) enforce the on/off status requirements of the thermal units. Constraints (34) and (35) limit the output region of units with upward and downward reserves. Constraints (36) and (37) represent the conservative reserve provision to meet all possible ramping scenarios in adjacent time slots.

$$P^A_{g,t} \le u^{A,nor}_{g,t}\cdot P^A_{g,max} + u^{A,dpr}_{g,t}\cdot P^A_{g,min} + u^{A,oil}_{g,t}\cdot P^A_{g,a} \tag{25}$$

$$P^A_{g,t} \ge u^{A,nor}_{g,t}\cdot P^A_{g,min} + u^{A,dpr}_{g,t}\cdot P^A_{g,a} + u^{A,oil}_{g,t}\cdot P^A_{g,b} \tag{26}$$

$$u^{A,nor}_{g,t} + u^{A,dpr}_{g,t} + u^{A,oil}_{g,t} = u^{A,ind}_{g,t} \tag{27}$$

$$P^A_{g,t} - P^A_{g,t-1} \le (u^{A,nor}_{g,t}\cdot R^{A,up}_{g,nor} + u^{A,dpr}_{g,t}\cdot R^{A,up}_{g,dpr} + u^{A,oil}_{g,t}\cdot R^{A,up}_{g,oil})\Delta t \tag{28}$$

$$P^A_{g,t} - P^A_{g,t-1} \ge -(u^{A,nor}_{g,t}\cdot R^{A,dn}_{g,nor} + u^{A,dpr}_{g,t}\cdot R^{A,dn}_{g,dpr} + u^{A,oil}_{g,t}\cdot R^{A,dn}_{g,oil})\Delta t \tag{29}$$

$$u_{g,t}^{A,ind} - u_{g,t-1}^{A,ind} = u_{g,t}^{A,su} - u_{g,t}^{A,sd} \tag{30}$$

$$u_{g,t}^{A,su} + u_{g,t}^{A,sd} \leq 1 \tag{31}$$

$$\sum_{\tau=t}^{t+\tau_g^{A,on}-1} u_{g,\tau}^{A,su} \leq u_{g,t}^{A,ind} \tag{32}$$

$$\sum_{\tau=t}^{t+\tau_g^{A,off}-1} u_{g,\tau}^{A,sd} \leq 1 - u_{g,t}^{A,ind} \tag{33}$$

$$P_{g,t}^{A} + r_{g,t}^{A,up} \leq u_{g,t}^{A,ind} \cdot P_{g,max}^{A} \tag{34}$$

$$P_{g,t}^{A} - r_{g,t}^{A,dn} \geq u_{g,t}^{A,ind} \cdot P_{g,b}^{A} \tag{35}$$

$$\left(P_{g,t}^{A} + r_{g,t}^{A,up}\right) - \left(P_{g,t-1}^{A} - r_{g,t-1}^{A,dn}\right) \leq (u_{g,t}^{A,nor} \cdot R_{g,nor}^{A,up} + u_{g,t}^{A,dpr} \cdot R_{g,dpr}^{A,up} + u_{g,t}^{A,oil} \cdot R_{g,oil}^{A,up})\Delta t \tag{36}$$

$$\left(P_{g,t}^{A} - r_{g,t}^{A,dn}\right) - \left(P_{g,t-1}^{A} + r_{g,t-1}^{A,up}\right) \geq -(u_{g,t}^{A,nor} \cdot R_{g,nor}^{A,dn} + u_{g,t}^{A,dpr} \cdot R_{g,dpr}^{A,dn} + u_{g,t}^{A,oil} \cdot R_{g,oil}^{A,dn})\Delta t \tag{37}$$

3.3.3. Battery Storage Constraints

In the planning stage, the number of optimal storage deployments is treated as a decision variable. Other parameters, such as the maximum charge/discharge rates and the depth of discharge, are assumed to be proportional to the optimized capacity. Constraint (38) ensures that storage does not charge and discharge simultaneously. Eqs. (39) and (40) limit the charging and discharging power. Constraint (41) is the secure range of energy level. Eq. (42) defines the actual storage capacity accounting for aging. Constraint (43) is the dynamic equation of the energy level. Constraint (44) represents the relationship between the installed storage capacity and the capacity of a single storage unit. Storage can supply upward reserves by increasing the discharging or decreasing the charging power. The upward reserve available is constrained by (45). Similarly, constraint (46) limits the downward reserve available. Constraints (47) and (48) represent conservative continuation reserves provisions of storage.

$$u_t^{A,c} + u_t^{A,d} \leq 1 \tag{38}$$

$$0 \leq P_t^{A,c} \leq u_t^{A,c} P_{max}^{A,c} \tag{39}$$

$$0 \leq P_t^{A,d} \leq u_t^{A,d} P_{max}^{A,d} \tag{40}$$

$$E^A_{min} \le E^A_t \le E^{A,real}_t \tag{41}$$

$$E^{A,real}_t = E^{A,real}_{t-1} - \Lambda^{A,cal}_t - \Lambda^{A,cyc}_t,\ E^{A,real}_0 = E^A_{max} \tag{42}$$

$$E^A_t = E^A_{t-1} + \left(\eta^{A,c} P^{A,c}_t - P^{A,d}_t / \eta^{A,d}\right) \Delta t \tag{43}$$

$$E^A_{max} = n^A E^{cap} \tag{44}$$

$$0 \le r^{A,e,up}_t \le P^{A,d}_{max} - P^{A,d}_t + P^{A,c}_t \tag{45}$$

$$0 \le r^{A,e,dn}_t \le P^{A,c}_{max} - P^{A,c}_t + P^{A,d}_t \tag{46}$$

$$E^A_t - \sum\nolimits_{\tau=1}^{t} r^{A,e,up}_\tau / \eta^{A,d} \ge E^A_{min} \tag{47}$$

$$E^A_t + \sum\nolimits_{\tau=1}^{t} r^{A,e,dn}_\tau \eta^{A,c} \le E^A_{max} \tag{48}$$

3.3.4. HVDC Deliverable Flexibility-sharing Constraints

HVDC tie-lines do not inherently provide flexibility, but they enable the sharing of flexibility across regions, which contributes to reducing investment costs. Limited by physical and adjustable capacities, the deliverability should be considered in the operation model. The schematic diagram of the flexibility-sharing is shown in Fig.5.

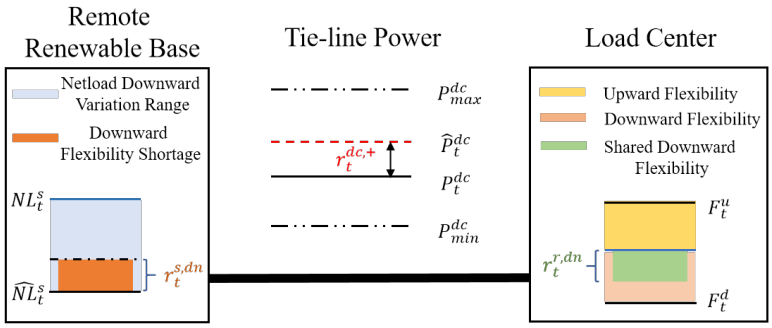

Fig. 5. Schematic diagram of the flexibility-sharing via HVDC tie-line.

Constraint (49) defines the limit of physical transmission power of the HVDC tie-line. Constraint (50) prevents significant changes in transmission power between adjacent time slots. Eq. (51) is the annual transmitted electricity, which can be either pre-determined or optimized. Constraints (52) and (53) limit the transmission power with exportable reserves. Constraints (54) and (55) ensure that transmission adjustments, considering conservative exportable reserves, remain

within physical limits.

$$P_{min}^{dc} \leq P_t^{dc} \leq P_{max}^{dc} \tag{49}$$

$$R^{dc,dn} \leq P_t^{dc} - P_{t-1}^{dc} \leq R^{dc,up} \tag{50}$$

$$\sum\nolimits_{t \in \mathcal{Y}} P_t^{dc} \Delta t = Q^{dc} \tag{51}$$

$$P_t^{dc} + r_t^{dc,+} \leq P_{max}^{dc} \tag{52}$$

$$P_t^{dc} - r_t^{dc,-} \geq P_{min}^{dc} \tag{53}$$

$$\left(P_t^{dc} + r_t^{dc,+}\right) - \left(P_{t-1}^{dc} - r_{t-1}^{dc,-}\right) \leq R^{dc,up} \tag{54}$$

$$\left(P_t^{dc} - r_t^{dc,-}\right) - \left(P_{t-1}^{dc} + r_{t-1}^{dc,+}\right) \geq -R^{dc,dn} \tag{55}$$

The deliverable flexibility is constrained not only by the HVDC tie-line but also by the available flexibility at the sending and receiving ends. It is modeled in (56)-(59).

$$r_t^{s-r,up} \leq r_t^{dc,+} \leq r_t^{s,e,up} + \sum\nolimits_{g \in \mathcal{G}^s} r_{g,t}^{s,up} \tag{56}$$

$$r_t^{s-r,dn} \leq r_t^{dc,-} \leq r_t^{s,e,dn} + \sum\nolimits_{g \in \mathcal{G}^s} r_{g,t}^{s,dn} \tag{57}$$

$$r_t^{r-s,up} \leq r_t^{dc,-} \leq r_t^{r,e,up} + \sum\nolimits_{g \in \mathcal{G}^r} r_{g,t}^{r,up} \tag{58}$$

$$r_t^{r-s,dn} \leq r_t^{dc,+} \leq r_t^{r,e,dn} + \sum\nolimits_{g \in \mathcal{G}^r} r_{g,t}^{r,dn} \tag{59}$$

Given that flexibility can be shared solely in one direction during each time slot, exportable flexibility must satisfy constraints (60) and (61).

$$r_t^{s-r,up} \cdot r_t^{r-s,up} = 0 \tag{60}$$

$$r_t^{s-r,dn} \cdot r_t^{r-s,dn} = 0 \tag{61}$$

Note that the framework applies differently to line-commutated converter (LCC) and modular multilevel converter (MMC) HVDC systems. For LCC, it optimizes steady-state power schedules to enhance existing asset utilization. For MMC, the framework enables the joint optimization of energy transfer and dynamic ancillary services. Although the framework is formulated

generically, it is particularly well-suited to inform planning and investment decisions for future MCC-dominated power systems.

3.3.5. *Probabilistic Reserve Provision for Uncertain Interval*

In practice, to ensure the robustness of the planning strategy, inter-regional flexibility must be sufficient to accommodate net-load uncertainty. Constraints (62) and (63) define the upward and downward reserve satisfaction at the sending end. Constraints (64) and (65) represent the upward and downward reserve provision for the receiving end. It ensures that the reserve provisions are sufficient to accommodate net-load variations under a specified confidence level α.

$$\sum\nolimits_{g\in\mathcal{G}^s} r_{g,t}^{s,up} + r_t^{s,e,up} + r_t^{r-s,up} - r_t^{s-r,up} \geq \overline{\epsilon}_{t,\alpha}^{s,nl} \tag{62}$$

$$\sum\nolimits_{g\in\mathcal{G}^s} r_{g,t}^{s,dn} + r_t^{s,e,dn} + r_t^{r-s,dn} - r_t^{s-r,dn} \geq \underline{\epsilon}_{t,\alpha}^{s,nl} \tag{63}$$

$$\sum\nolimits_{g\in\mathcal{G}^r} r_{g,t}^{r,up} + r_t^{r,e,up} + r_t^{s-r,up} - r_t^{r-s,up} \geq \overline{\epsilon}_{t,\alpha}^{r,nl} \tag{64}$$

$$\sum\nolimits_{g\in\mathcal{G}^r} r_{g,t}^{r,dn} + r_t^{r,e,dn} + r_t^{s-r,dn} - r_t^{r-s,dn} \geq \underline{\epsilon}_{t,\alpha}^{r,nl} \tag{65}$$

where $\overline{\epsilon}_{t,\alpha}^{s,nl}$, $\underline{\epsilon}_{t,\alpha}^{s,nl}$, $\overline{\epsilon}_{t,\alpha}^{r,nl}$, and $\underline{\epsilon}_{t,\alpha}^{r,nl}$ represent the upper and lower bounds of net load prediction errors under a confidence level α at the sending and receiving ends, respectively.

Finally, the planning model of the inter-regional power system with operational constraints is formulated as a mixed-integer nonlinear programming (MINLP), given as **P**.

$$\mathbf{P}: \min\ \hat{f} = \frac{\gamma(1+\gamma)^Y}{(1+\gamma)^Y - 1} \sum_{A\in\{s,r\}} \left\{ c_e^{inv} E_{max}^A + c_p^{inv} P_{max}^{A,c} - c_e^{rec} E_T^A \right\} + \sum_{A\in\{s,r\}} \sum_{t\in\mathcal{Y}} \sum_{g=1}^{Ng} \hat{c}(P_{g,t}^A) \tag{66}$$

$$\text{s.t. } (8) - (13), (20) - (65).$$

It is noted that the bilinear terms in constraints (13), (39), (40), (60), and (61) can be linearized by the Big-M method. $\Lambda_t^{A,cyc}$ is linearized into the following constraints.

$$0 \leq \Lambda_t^{A,cyc} \leq M \cdot u_t^{A,d} \tag{67}$$

$$\Lambda_t^{A,cyc} \leq (\Lambda_t^{A,temp} - \Lambda_{t-1}^{A,temp}) + M \cdot (1 - u_t^{A,d}) \tag{68}$$

$$\Lambda_t^{A,cyc} \geq (\Lambda_t^{A,temp} - \Lambda_{t-1}^{A,temp}) - M \cdot (1 - u_t^{A,d}) \tag{69}$$

Let $z_t^{A,c}$ and $z_t^{A,d}$ represent $u_t^{A,c} P_{max}^{A,c}$ and $u_t^{A,d} P_{max}^{A,d}$, respectively, then constraints (39) and (40) are converted into the following set of mixed-integer linear constraints.

$$z_t^{A,c} \leq P_{max}^{A,c} \tag{70}$$

$$z_t^{A,c} \geq P_{max}^{A,c} - M(1 - u_t^{A,c}) \tag{71}$$

$$0 \leq z_t^{A,c} \leq M u_t^{A,c} \tag{72}$$

$$z_t^{A,d} \leq P_{max}^{A,d} \tag{73}$$

$$z_t^{A,d} \geq P_{max}^{A,d} - M(1 - u_t^{A,d}) \tag{74}$$

$$0 \leq z_t^{A,d} \leq M u_t^{A,d} \tag{75}$$

By introducing binary indicators δ_t^{up} and δ_t^{dn}, constraints (60) and (61) are transformed into the following equivalent mixed-integer linear constraints.

$$0 \leq r_t^{s-r,up} \leq M \delta_t^{up} \tag{76}$$

$$0 \leq r_t^{r-s,up} \leq M(1 - \delta_t^{up}) \tag{77}$$

$$0 \leq r_t^{s-r,dn} \leq M \delta_t^{dn} \tag{78}$$

$$0 \leq r_t^{r-s,dn} \leq M(1 - \delta_t^{dn}) \tag{79}$$

$$\delta_t^{up}, \delta_t^{dn} \in 0, 1 \tag{80}$$

Then, the original **P** is recast as an **MILP** that commercial solvers can efficiently solve.

MILP : min $\hat{f}$

s.t. (8), (10) – (13), (20) – (38), (44) – (59), (62) – (65), and (67) – (80).

4. Case Study

To explore the efficiency and effectiveness of the proposed model and method, case studies are carried out on two inter-regional power systems. All case studies are implemented with MATLAB and solved with GUROBI 10.0.0. The simulations are executed on a PC equipped with an Intel(R) Core(TM) i5-9500 3.00 GHz CPU and 32 GB of memory.

4.1. Two-area HVDC-linked System

The system comprises four thermal units at both the sending and receiving ends. The parameters of the thermal units are listed in Table 2. The simulation is conducted using four typical seasonal scenarios, each with 24 time slots. The RRB includes a wind farm with a capacity of 1,500 MW and PV with a capacity of 1,000 MW. Both the sending and receiving ends have loads with peaks of 2,000 MW. The minimum energy level and full charge time, associated with the installed storage capacity, are set to 0.1 and 2h. The storage cycling efficiency is set to 0.9. The unit investment cost of storage is 3 million CNY/MWh. The transmission capacity and adjustment amplitude of the tie-line are 2,000 MW and 500 MW, respectively. The number of linearized segments is set to 10, based on 1,000 sampled points within the operational range.

Table 2: Parameters of thermal units in the inter-regional power system.

$P^{A}_{g,min}(MW)$	$\tilde{P}^{A}_{g,min}(MW)$	$P^{A}_{g,max}(MW)$	$R^{A,up}_{g}/R^{A,dn}_{g}(MW/h)$	$a_g(10^{-3}CNY/MW^{-2})$	$b_g(CNY/MW^{-1})$	$c_g(CNY)$
125	50	300	75	3.03	102.19	6311.80

4.1.1. Uncertain Interval Prediction

Historical weather, load, and renewable generation data are used to construct the data-informed operational uncertain intervals. Each seasonal data set is divided into 80% for training and 20% for testing. Point predictions are generated using a GRU network. Prediction errors are evaluated on the testing data set. A confidence level of 90% is applied to construct the uncertain prediction intervals. The learning rate is 0.01. The maximum iteration times are 50,000. Figs. 6 and 7 illustrate the net-load points predicted in 24-hours and the corresponding prediction intervals for four representative seasonal scenarios at the sending and receiving ends, respectively. These figures show

the seasonal variability of net load uncertainty and the prediction intervals that capture the range of possible net load realizations. The prediction intervals serve as the basis for the subsequent planning of flexible resources and reserve allocation.

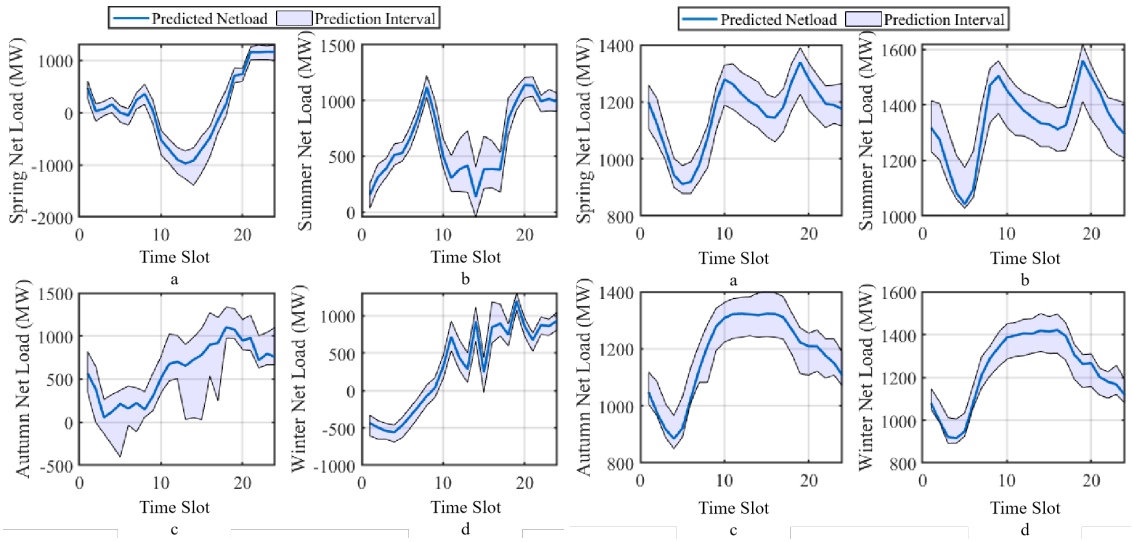

Fig. 6. Sending-end prediction intervals of net load. (a) Spring scenario. (b) Summer scenario. (c) Autumn scenario. (d) Winter scenario.

Fig. 7. Receiving-end prediction intervals of net load. (a) Spring scenario. (b) Summer scenario. (c) Autumn scenario. (d) Winter scenario.

4.1.2. Effectiveness of Flexibility-sharing

The dispatch results of the reserve provision at the receiving end are presented in Fig.8. The solid red and blue lines represent the demand for upward and downward flexibility, respectively. It is observed that the reserve provision marginally exceeds the flexibility demand in certain time slots. These surplus reserves are exportable and can be shared with other regions. In the fall season, upward reserve surpluses occur in the 18th time slot, mainly supported by thermal units. The downward reserve surpluses occur in the 14th time slot. Storage provides downward reserves at 16:00, 21:00, and 23:00. The surplus reserves are delivered to the sending end during certain time slots.

1) Cost Reduction: The efficacy of the bidirectional flexibility-sharing model is evaluated against a benchmark model in which the tie-line does not transfer flexibility. Table 3 lists the optimized storage deployment and the total annual investment and operational costs.

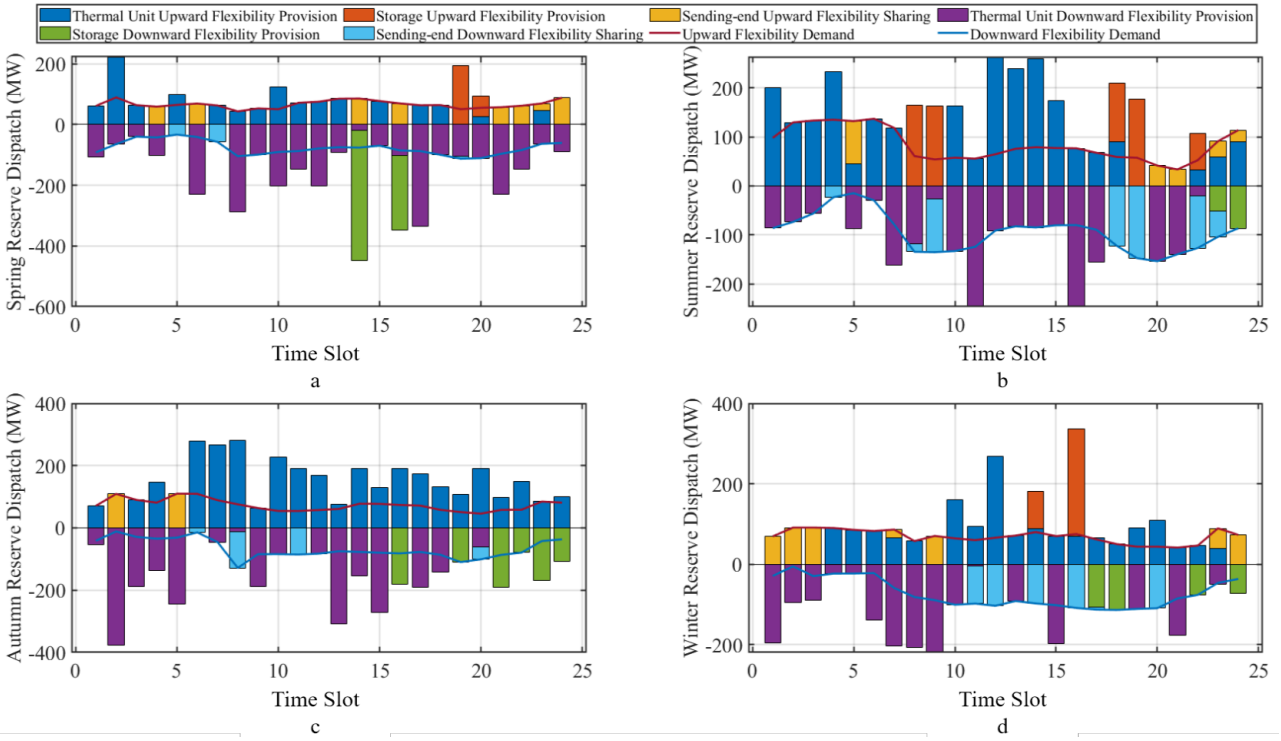

Fig. 8. The reserve provision strategy of 4 seasonal classical scenarios at the receiving end. (a) Spring scenario. (b) Summer scenario. (c) Autumn scenario. (d) Winter scenario.

Table 3: The optimized storage deployment and total cost of two cases.

Model	Sending-end (MWh)	Receiving-end (MWh)	Total cost (CNY)
Benchmark	2,400	1,100	2.657×10^9
Proposed model	1,200	1,100	2.524×10^9

It is observed that both the deployed storage capacity and the total cost under the proposed model are lower than those of the benchmark model. In the proposed model, the optimized storage deployment at the sending end is 1,200 MWh, compared to 2,400 MWh in the benchmark case. In addition, the optimized storage capacity at the receiving end is 1,100 MWh in both models. The combined deployed capacity at both ends is reduced by 34.29% compared to the benchmark model. This suggests that flexibility sharing via the tie-line can help reduce the need for storage investment. Furthermore, the total investment and operational costs under the proposed model are lower than those of the benchmark model. For example, the total annual cost is reduced by 5.16%. The main cost savings are due to the reduced storage investment. It indicates that flexibility-sharing in the proposed model contributes to improved economic efficiency.

2) Deliverability: Limited by the adjustment and capacity limits of the HVDC tie-line, not all available flexibility can be delivered to the desired end. To demonstrate the effectiveness of the proposed model, we compare it with a model that omits deliverability considerations. For example, at the sending end, the upward flexibility-sharing constraint is formulated as $r_t^{s-r,up} \leq r_t^{s,e,up} + \sum_{g\in\mathcal{G}^s} r_{g,t}^{s,up}$, instead of (56).

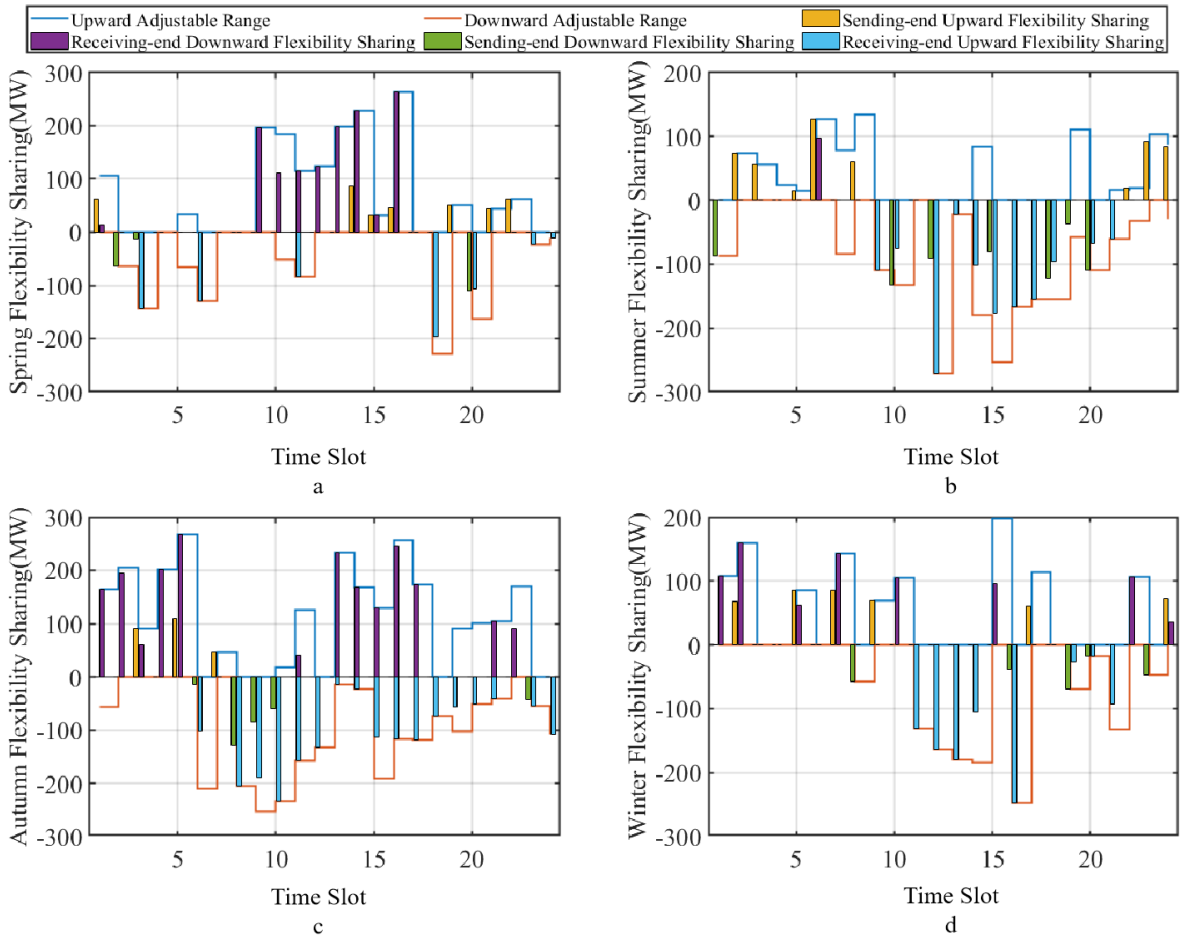

Fig. 9. The tie-line adjustable ranges and scheduled flexibility in 4 seasonal scenarios considering deliverability. (a) Spring scenario. (b) Summer scenario. (c) Autumn scenario. (d) Winter scenario.

Fig.9 shows the adjustable power ranges of the HVDC tie-line and the scheduled flexibility considering the deliverability in four seasonal scenarios. It is observed that all shared flexibilities are within the adjustable ranges of the HVDC tie-line in both upward and downward directions. However, if deliverability constraints are not incorporated, reserve provisions may not be fully delivered to the desired end. As shown in Fig.10, the scheduled reserve for sharing from 12:00 to

14:00 and 16:00 exceeds the adjustable range of the tie-line. In other words, these reserves cannot be delivered. Thus, incorporating deliverability constraints is essential to ensure that flexibility is fully available for uncertainty management.

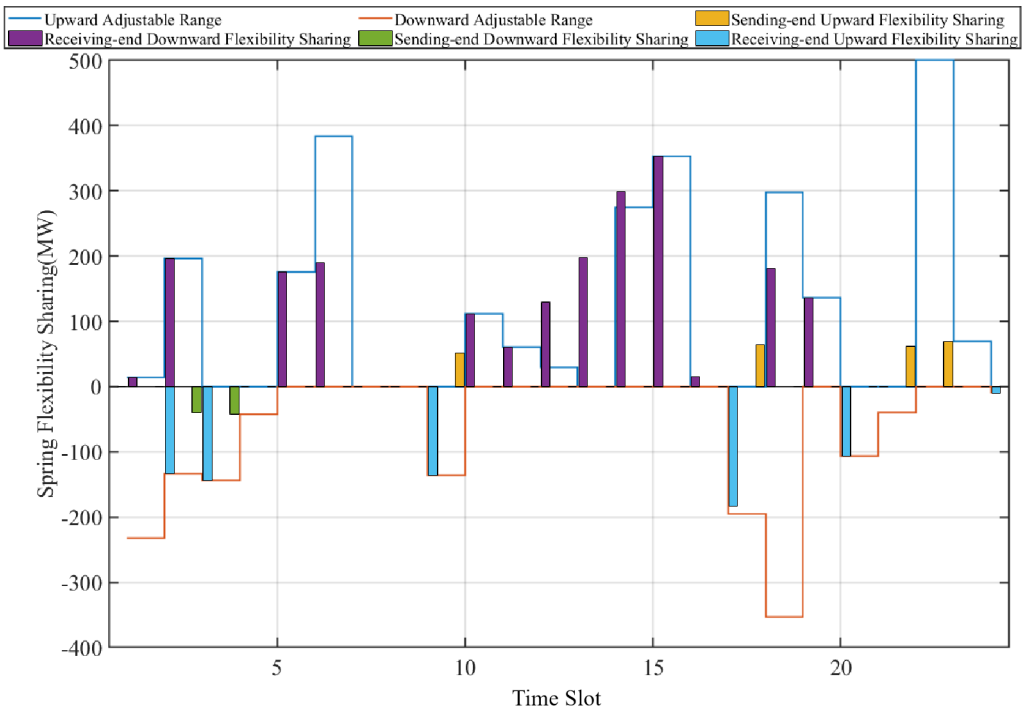

Fig. 10. The tie-line adjustable ranges and scheduled flexibility in the spring scenario without considering deliverability.

4.1.3. Robustness of Interval-based Planning

In this section, 100 Monte Carlo simulations are conducted to evaluate the robustness of the planning results. The 100 scenarios are randomly sampled within the prediction intervals using the formula $\hat{d}_{i,t} = \underline{d}_{i,t} + \gamma \cdot (\overline{d}_{i,t} - \underline{d}_{i,t})$, where γ is a random variable uniformly distributed between 0 and 1. $\overline{d}_{i,t}$ and $\underline{d}_{i,t}$ represent the upper and lower bounds of the net-load prediction interval. The proposed interval prediction-based planning approach is compared with a point prediction-based planning strategy. The results of planning and operational performance are summarized in Table 4.

Table 4 shows that the storage capacities derived from the point prediction method are 600 MWh and 500 MWh, while the interval prediction method yields 1,200 MWh and 1,100 MWh. This difference arises because the point prediction method utilizes deterministic optimization,

Table 4: The planning and operation performance of point-based and interval-based methods.

Model	Sending-end installed storage (MWh)	Receiving-end installed storage (MWh)	Annual total cost (CNY)	# Infeasible scenarios
Point-based	600	500	2.370×10^9	57
Interval-based	1,200	1,100	2.524×10^9	0

whereas the interval prediction approach deploys additional storage to accommodate uncertainties. The annual total cost under the point-based method is lower than that under the interval-based method. This is mainly due to differences in installed storage capacities. It shows that the point prediction-based method results in 57 infeasible scenarios, while the interval prediction-based method achieves feasibility in all scenarios. This indicates that the interval prediction-based approach provides sufficient flexibility by deploying adequate storage for the safe operation of inter-regional power systems.

4.1.4. Impact of Probabilistic Prediction Confidence Levels

The uncertainty prediction interval is determined under the confidence level α. To investigate its impact on planning results, simulations are conducted using different confidence levels ranging from 81% to 99%. The deployed storage capacities and total costs are shown in Fig.11. (a). It shows that the total deployed storage capacities of the inter-regional power system increase as the confidence levels rise. It suggests that additional storage is required to accommodate the larger uncertainty associated with higher confidence levels. The total annual cost exhibits a similar increasing trend.

Since the confidence level significantly influences the deployment of flexible resources, selecting an appropriate confidence level is crucial for inter-regional planning. Marginal impact is usually used to determine the suitable confidence level. Here, the criterion is defined as the ratio of total cost to the confidence level. The marginal costs are shown in Fig. 11. (b). It is observed that the minimum marginal cost occurs at a confidence level of 91%. Thus, 91% is considered the most suitable choice in this case. Interestingly, strategies with confidence levels ranging from 88% to 94% exhibit similar marginal costs. From a robustness perspective, a confidence level of 94% is also acceptable, as it can accommodate a larger range of uncertainties.

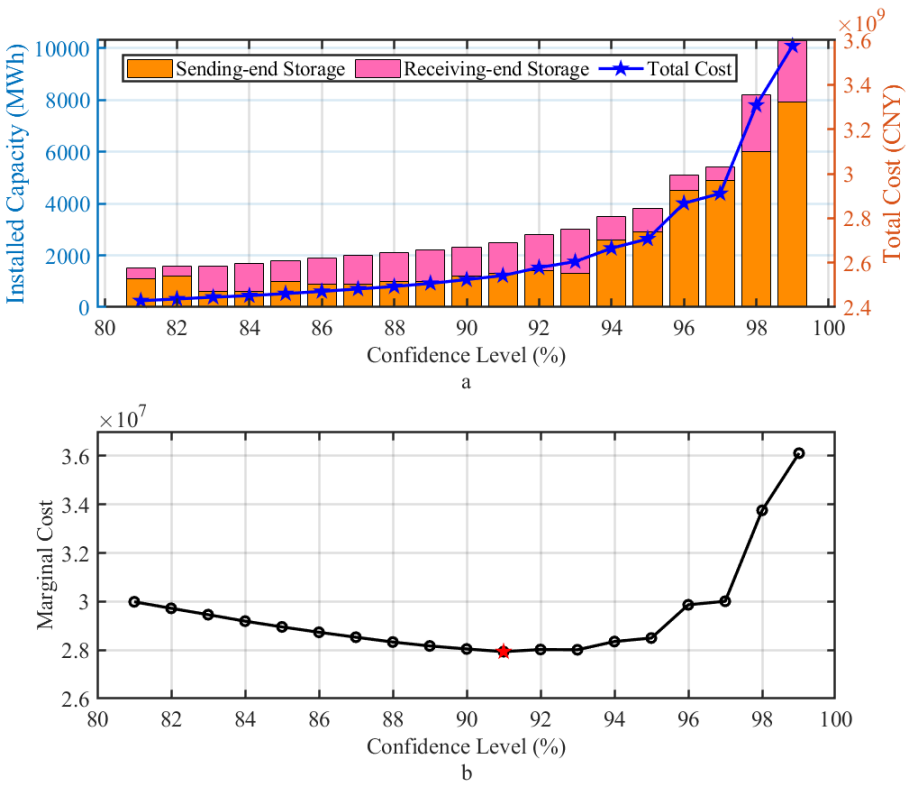

Fig. 11. Comparison of the optimized storage capacities, total costs, and marginal cost under different confidence levels. (a) Optimized storage capacities and the corresponding total costs. (b) Marginal cost.

4.1.5. Impact of Least-Square Linearized Segments

The performance of the piecewise approximation is assessed through simulations using 10, 20, 40, and 80 linear segments. The results, including deployed storage capacities, annual total costs, and solution times, are summarized in Table 5. It is observed that the optimized storage capacities remain consistent across different numbers of segments. Additionally, the annual total costs decrease as the linearization becomes more accurate, as the boundary values of the divided segments tend to be overestimated. However, the computation time increases significantly as the number of linearized segments increases. When the number of segments is doubled or quadrupled, the solution time increases by 2.48 and 5.09 times, respectively. In particular, an eightfold increase in the number of segments results in an approximately 47-fold increase in solution time. The objective mismatches corresponding to different numbers of linearized segments are summarized in the last column of Table 5. For the case with 10 segments, the approximation error in the objective

function is approximately 0.28%. As the number of segments increases, the approximation error decreases and gradually approaches zero. This suggests that an appropriate choice of linearized segments can achieve a near-optimal solution while maintaining acceptable computation time and solution accuracy.

Table 5: The model performance under different linearized segments.

# Linearized segments	Sending-end installed storage (MWh)	Receiving-end installed storage (MWh)	Annual total cost (CNY)	Solution time (s)	Objective error
10	1,200	1,100	2.524×10^9	47.63	0.28%
20	1,200	1,100	2.521×10^9	118.04	0.04%
40	1,200	1,100	2.521×10^9	242.31	0.008 %
80	1,200	1,100	2.521×10^9	2,249.35	0.001%

To further evaluate the accuracy of the linear approximation, the discrepancies between the original nonlinear function and its piecewise linear approximation with 20 segments are illustrated in Fig. 12(a). It is observed that the approximated curve closely follows the original function. As shown in Fig. 12(b), all approximation errors are below 1.26%, with a root mean square error of approximately 0.29%. These results indicate that the piecewise linear approximation with 20 segments provides a sufficiently accurate representation of the original nonlinear function, making it suitable for use in the proposed optimization model.

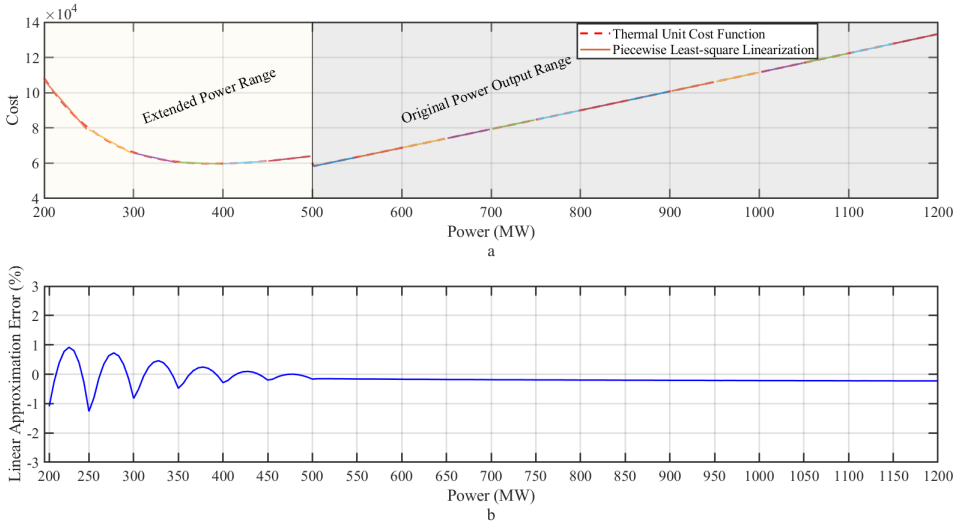

Fig. 12. The linear approximation of thermal unit cost. (a) Original nonlinear function with 10 approximated segments. (b) Approximation errors.

4.1.6. Impact of Conservative Levels on Robustness

All the cases described above are conducted under the most conservative conditions, which assume 24 hours of continuous upward and downward reserves. However, it is overly conservative as such scenarios have a low probability in practice. To balance economic efficiency and reliability, the impact of different conservative levels on robustness is analyzed. First, the optimized storage capacities are obtained under different conservative levels. Then, 100 Monte Carlo scenarios are sampled, and the number of infeasible scenarios is counted.

Table 6: The performance of storage deployment strategies under different conservative levels.

Conservatism Level (continuous hours)	Sending-end installed storage (MWh)	Receiving-end installed storage (MWh)	Annual total cost (CNY)	# Infeasible scenarios	Feasibility Ratio
1 2	600	800	2.413×10^9	13	87%
3	800	900	2.423×10^9	4	96%
4 6	1,200	700	2.448×10^9	0	100%
8 12 24	1,200	1,100	2.524×10^9	0	100%

Table 7: The reserve duration for different continuous hours in 100 Monte Carlo simulation scenarios.

Reserve Duration	1	2	3	4	5	6	7	8-24
Sending end & Spring	60.38%	28.17%	8.81%	2.06%	0.52%	0.06%	0	0
Sending end & Summer	58.23%	30.89%	8.56%	1.94%	0.32%	0.06%	0	0
Sending end & Autumn	61.15%	27.56%	8.02%	2.82%	0.45%	0	0	0
Sending end & Winter	59.92%	29.99%	7.19%	1.94%	0.90%	0	0.06%	0
Receiving end & Spring	59.42%	30.52%	7.50%	1.92%	0.64%	0	0	0
Receiving end & Summer	59.19%	27.89%	9.78%	2.69%	0.32%	0.13%	0	0
Receiving end & Autumn	59.88%	28.41%	8.58%	2.28%	0.65%	0.13%	0.07%	0
Receiving end & Winter	60.08%	29.97%	7.46%	1.91%	0.45%	0.13%	0	0

The detailed results are summarized in Table 6. It is observed that the total optimized storage capacity grows as the conservative level increases. Consequently, the total annual cost also increases. The number of infeasible scenarios decreases as the conservative level increases. Interestingly, identical storage capacities are deployed at certain conservative levels. For example,

conservative levels of 8, 12, and 24 continuous hours result in storage capacities of 1,200 MWh and 1,100 MWh at the sending and receiving ends, respectively. It shows that no infeasible scenarios occur when the conservative level exceeds 3 time slots. This is because only a few 3-hour continuous upward or downward flexibility requirements in the simulated cases. In other words, a 4-hour continuous flexibility provision is enough to deal with uncertainties in practice. It indicates that a moderate conservative level can effectively balance overall cost and operational robustness.

To provide beyond case-specific observations, additional statistical analyses are conducted to examine the duration characteristics of reserve events. The feasibility ratios of the planning results, obtained from Monte Carlo simulations, are reported in the last column of Table 6. Table 7 presents the probabilities that upward or downward reserve events persist in the same direction over multiple consecutive time slots at both the sending and receiving ends in four seasonal scenarios. The results show that approximately 80–90% of reserve events last for no more than two consecutive time slots. The remaining 10% of events persist for three to seven time slots, corresponding to the most relevant operational scenarios, such as multi-hour cloud movement or sustained weather-induced net load variations. Reserve events extending beyond seven consecutive time slots are extremely rare. These findings are consistent with the planning results of the proposed model and further support the robustness and practical applicability of the proposed planning strategy at moderate conservativeness levels.

4.2. HVDC-linked System Constructed by Two IEEE 39-bus Systems

In this section, the proposed model and method are applied to a two-area HVDC-linked test system, each area based on an IEEE 39-bus system comprising 10 thermal units and 46 branches. The HVDC link connects bus-39 at the sending end to bus-1 at the receiving end. PV and wind generation are located at bus-39 of the sending area, with profiles identical to those in the previous case but scaled by factors of 4 and 2, respectively. The peak loads at the sending and receiving ends are 2,500 MW and 12,500 MW, respectively, and the HVDC transmission capacity is 8,000 MW. Other parameters are consistent with those of the previous case.

4.2.1. *Effectiveness of the Temporal Correlated Prediction Interval*

In this work, a temporally correlated prediction interval framework is proposed for long-term storage sizing, combining a GRU-based point forecast with conditional KDE. The conditional KDE applies a Gaussian kernel with a bandwidth of 5 for multi-hour error trajectories and a Silverman-rule bandwidth at the time-step level for conditional density estimation. The method assumes local stationarity under similar error trajectories and implicitly captures temporal correlations through trajectory-based weighting. To evaluate the effectiveness of the proposed approach, the prediction intervals that account for the temporal correlation are compared with those obtained using the traditional KDE-based method.

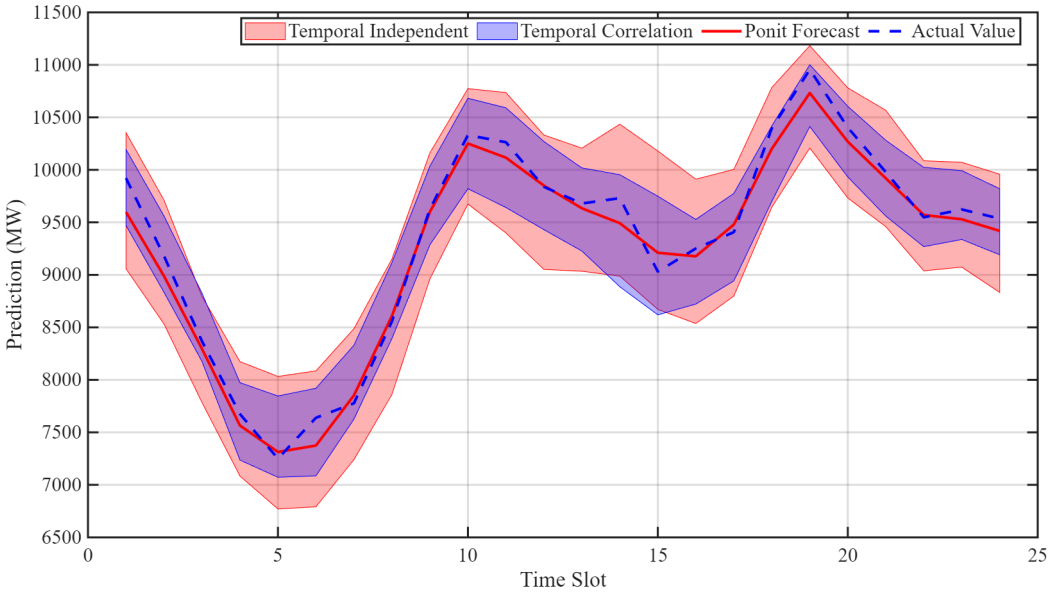

Fig. 13. The temporal correlated prediction interval based on the conditional KDE in the spring scenario at the receiving end.

Fig. 13 illustrates the prediction intervals obtained using the proposed temporally correlated approach and the conventional KDE method, which neglects temporal correlation, for the spring scenario at the receiving end. It is observed that the temporally correlated prediction interval not only fully covers the actual 24-hour spring net load, but is also narrower than that produced by the conventional KDE method. It indicates that incorporating temporal correlation yields a narrower prediction interval, helping to reduce the influence of low-probability scenarios.

To further evaluate the quality of the predicted uncertainty intervals, several widely used pre-

dictive interval metrics are used, including the Prediction Interval Coverage Probability (PICP), the Prediction Interval Normalized Averaged Width (PINAW), and the Coverage Width-based Criterion (CWC). These metrics enable a quantitative assessment of both the reliability and sharpness of the prediction intervals. Specifically, PICP measures the proportion of actual values that fall within the interval, PINAW evaluates the relative width of the interval, and CWC combines coverage and width to provide a balanced performance metric.

Table 8: The performance of different interval prediction methods under the confidence level of 90%.

Method	PICP	PINAW	CWC
conditional KDE	90.64%	0.238	0.3946
conventional KDE	91.88%	0.405	0.5504
quantile regression	93.07%	0.352	0.4226
Bootstrap	92.34%	0.478	0.6150

To demonstrate the effectiveness of the proposed method, the GRU–conditional KDE intervals are compared with those obtained from other non-parametric approaches, including conventional KDE, quantile regression, and Bootstrap. The performance metrics of the prediction intervals are summarized in Table 8. All methods achieve a PICP greater than 90%, indicating adequate reliability. In particular, conditional KDE produces the narrowest intervals, with a PINAW of 0.238, substantially smaller than the 0.405 of conventional KDE, 0.352 of quantile regression, and 0.478 of Bootstrap. Although conditional KDE has a slightly lower PICP than some alternatives, it attains the lowest CWC value, demonstrating a superior tradeoff between coverage and compactness. These results indicate that conditional KDE provides reliable but tighter prediction intervals, making it particularly suitable for long-term flexibility planning by minimizing the overestimation of storage or reserve requirements.

4.2.2. Effectiveness of the Planning Model

To further investigate the scalability and computational complexity of the proposed joint planning–operation model, a comparative study is conducted between a two-area system without internal network constraints and an HVDC-linked system composed of two IEEE 39-bus networks. Since the HVDC link supplies power from a remote renewable base to a limited portion of the receiving end power system, the IEEE 39-bus system is adopted to represent the local network at

both the sending and receiving ends. For each case, key computational indicators, including the number of decision variables, the number of constraints, the solution time, and the use of memory, are recorded and analyzed to evaluate the scalability of the model.

Table 9: Computational complexity analysis.

Model	# Var.	# Cons.	# Int.	Time	Peak Memory	Obj. (annual)
Two-area system without network	60,106	148,594	32.066	251.07 s	1.95 GB	8.198×10^9 CNY
HVDC-linked two IEEE 39-bus system	60,106	166,258	32.066	302.58 s	2.99 GB	8.210×10^9 CNY

In the proposed model, multiple binary variables are introduced to convert the intractable MINLP problem into a solvable MILP. Based on theoretical analysis, the number of decision variables scales as $O(G \cdot T \cdot L + 4G \cdot T + 2T \cdot M + 6T)$. From a computational perspective, although MILP problems are NP-hard in general, the linear growth of variables and constraints with respect to G, T, L, and M implies that the proposed formulation remains tractable for large-scale planning applications when representative time periods and a moderate number of linearization segments are adopted.

Detailed scalability indicators are shown in Table 9. It shows that incorporating transmission network constraints increases the number of constraints from 148,594 to 166,258, while the numbers of decision variables and integer variables remain unchanged. The increase in constraints is the main factor that affects the solution efficiency. This impact can be significantly reduced using the method proposed in our previous work [35, 36]. This indicates that the added network modeling primarily affects the constraint formulation rather than the dimensionality of the decision variables. Consequently, the solution time increases moderately from 251.07 s to 302.58 s, and the maximum memory usage increases from 1.95 GB to 2.99 GB. Despite this moderate increase in computational burden, the model remains tractable for planning applications. Moreover, the close objective values obtained in both cases demonstrate that including network constraints refines feasibility without significantly affecting the overall economic outcome. These results suggest that the computational complexity of the proposed framework scales reasonably with network size and that the MILP-based formulation can effectively accommodate more detailed physical constraints while maintaining acceptable solution efficiency, supporting its applicability to larger inter-regional power systems.

5. Conclusion

5.1. Discussion of Findings

This paper proposes a data-aided planning framework for storage deployment in inter-regional power systems with embedded operational constraints. The framework improves planning robustness by employing a temporally correlated data-informed uncertainty prediction interval. Simulation results highlight the necessity of incorporating the temporal correlations in uncertainty intervals for inter-regional planning, which narrows prediction intervals and contributes to reduced planning costs. Illustrative cases demonstrate that the piecewise least-squares approximation can reduce the computation time compared to the nonlinear formulation. Flexibility-sharing contributes to reductions in total investment and operational costs. The results reveal the potential for cost savings by striking a suitable trade-off between flexible resource investment and the degree of conservatism for flexibility provision constraints.

5.2. Conclusion and Future Work

This paper explores the data-aided planning framework of an inter-regional power system with operational constraints.

5.2.1. Workflow Integration

The proposed uncertainty quantification serves as a data-informed operational robustness module within the flexibility planning framework. It can be conceptually integrated into established industrial workflows as an upstream uncertainty pre-processor. In practice, the generated uncertainty envelopes would be fed directly into the scenario generation or robust optimization modules of existing Energy Management Systems or Optimal Planning Systems.

5.2.2. Planning and Computational Scalability

The framework is established for multi-year planning scenarios and multi-region planning scenarios. Its MILP form ensures industrial solver compatibility, with standard relaxation and decomposition methods available for large-scale and real-world planning cases.

5.2.3. Future Work

There are still limitations to the proposed method. For example, the GRU network primarily captures uncertainties arising from short-term weather forecast errors and intra-day variability. It deserves further investigation to study the non-stationarity and regime-switching characteristics of renewable generation and to give a more advanced planning time-scale uncertainty interval for improving the solution quality.

CRediT authorship contribution statement

Weile Kong: Formal analysis, Investigation, Methodology, Software, Validation, Writing - original draft. **Hongxing Ye**: Conceptualization, Supervision, Writing - review & editing, Validation, Methodology. **Yinyin Ge**: Data curation, Visualization, Writing - original draft, Investigation, Methodology. **Zhidong Wang**: Investigation, Resources, Validation. **Yi Huang**: Funding acquisition, Validation. **Zhi An**: Formal analysis, Validation.

Declaration of Competing Interest

Authors Zhidong Wang, Yi Huang and Zhi An are employed by State Grid Economic and Technological Research Institute. The remaining authors declare that they have no known competing financial interests or personal relationships that could have appeared to influence the work reported in this paper.

Funding sources

This work was supported by the Science and Technology Program of State Grid Corporation of China (SGCC) under Grant 5100-202456011A-1-1-ZN.

References

[1] D. Xu and Z. Wu, "Enhancing uncertainty management in multi-area asynchronous grids via hvdc: A distributionally robust chance constrained unit commitment approach," *Electric Power Systems Research*, vol. 251, p. 112255, 2026.

[2] People's Daily, "The electricity highway, for instant clean power." https://www.gov.cn/yaowen/liebiao/202501/content_6996424.htm, 2025-01-06. Accessed 12/10,2025.

[3] China Central Television, "Securing energy future: Ultra-grids powering china's "14th five-year" vision." https://news.cctv.com/2025/11/22/ARTIe0KN3cYThjCmWEhCMol0251122.shtml, 2025-11-22. Accessed 12/10,2025.

[4] Norvento Enerxía, "Large-scale hvdc projects in the world." https://www.norvento.com/en/blog/large-scale-hvdc-projects-in-the-world/. Accessed Aug. 8th, 2025.

[5] Chinadaily, "Second phase of china's largest renewable energy base begins construction." https://www.chinadaily.com.cn/a/202310/25/WS653881d1a31090682a5ea9c0.html. Accessed Jan. 6th, 2025.

[6] X. Liang and M. Abbasipour, "HVDC transmission and its potential application in remote communities: Current practice and future trend," *IEEE Transactions on Industry Applications*, vol. 58, no. 2, pp. 1706–1719, 2022.

[7] W. Kong, H. Ye, N. Wei, D. Xing, S. Liu, and W. Chen, "Optimization of inter-regional flexible resources for renewable accommodation," in *2023 5th Asia Energy and Electrical Engineering Symposium (AEEES)*, pp. 30–34, 2023.

[8] J. Zhao, Y. Zhang, Z. Liu, W. Hu, and D. Su, "Distributed multi-objective day-ahead generation and hvdc transmission joint scheduling for two-area hvdc-linked power grids," *International Journal of Electrical Power & Energy Systems*, vol. 134, p. 107445, 2022.

[9] S. Jiang, S. Gao, G. Pan, Y. Liu, C. Wu, and S. Wang, "Congestion-aware robust security constrained unit commitment model for AC-DC grids," *Applied Energy*, vol. 304, p. 117392, 2021.

[10] S. Jiang, C. Wu, S. Gao, G. Pan, Y. Liu, X. Zhao, and S. Wang, "Robust frequency risk-constrained unit commitment model for ac-dc system considering wind uncertainty," *Renewable Energy*, vol. 195, pp. 395–406, 2022.

[11] S. Jiang, Q. Hu, F. Li, L. Bai, Y. Dong, and Z. Guo, "Unlock the flexibility of hvdc interconnected systems: An enhanced emergency frequency response-enforced unit commitment model," *IEEE Trans. Power Syst.*, vol. 40, no. 3, pp. 2451–2464, 2025.

[12] W. Lin, Z. Yang, J. Yu, L. Jin, and W. Li, "Tie-line power transmission region in a hybrid grid: Fast characterization and expansion strategy," *IEEE Transactions on Power Systems*, vol. 35, no. 3, pp. 2222–2231, 2020.

[13] S. Jiang, S. Gao, G. Pan, X. Zhao, Y. Liu, Y. Guo, and S. Wang, "A novel robust security constrained unit commitment model considering HVDC regulation," *Applied Energy*, vol. 278, p. 115652, 2020.

[14] H. Ye, C. Zhou, N. Wei, S. Liu, and D. Xing, "Inter-regional unit commitment and pv scheduling considering frequency constraints," *Electric Power Systems Research*, vol. 221, p. 109462, 2023.

[15] X. Fang, K. S. Sedzro, H. Yuan, H. Ye, and B.-M. Hodge, "Deliverable flexible ramping products considering spatiotemporal correlation of wind generation and demand uncertainties," *IEEE Transactions on Power Systems*, vol. 35, no. 4, pp. 2561–2574, 2020.

[16] H. Wang and Z. Bie, "Data-driven distributionally robust energy and reserve scheduling considering res flexibil-

ity," *IEEE Transactions on Power Systems*, vol. 40, no. 3, pp. 2438–2450, 2025.

[17] S. Sreekumar, K. Sharma, R. Bhakar, S. Simon, and A. Rana, "Multi interval zero carbon flexible ramp product," *Electric Power Systems Research*, vol. 212, p. 108258, 2022.

[18] R. Heydari and T. Barforoushi, "Hvdc/ hvac transmission network expansion planning in electricity markets in the presence of wind resources," *Electric Power Systems Research*, vol. 229, p. 110182, 2024.

[19] X. Guo, S. Lou, Z. Chen, and Y. Wu, "Flexible operation of integrated energy system with HVDC infeed considering multi-retrofitted combined heat and power units," *Applied Energy*, vol. 325, p. 119833, 2022.

[20] M. Moradi-Sepahvand and T. Amraee, "Hybrid ac/dc transmission expansion planning considering hvac to hvdc conversion under renewable penetration," *IEEE Transactions on Power Systems*, vol. 36, no. 1, pp. 579–591, 2021.

[21] B. Li and J. Li, "Probabilistic sizing of a low-carbon emission power system considering HVDC transmission and microgrid clusters," *Applied Energy*, vol. 304, p. 117760, 2021.

[22] X. Zhu, B. Zeng, H. Dong, and J. Liu, "An interval-prediction based robust optimization approach for energy-hub operation scheduling considering flexible ramping products," *Energy*, vol. 194, p. 116821, 2020.

[23] Q. Wu, B. Han, M. Shahidehpour, C. Qi, G. Li, K. Wang, and L. Luo, "Extreme bifurcation interval with deep pv penetration considering correlated net bus load forecast errors," *IEEE Transactions on Sustainable Energy*, vol. 11, no. 4, pp. 2063–2076, 2020.

[24] F. Dong, J. Wang, H. Xu, and X. Zhang, "A robust real-time energy scheduling strategy of integrated energy system based on multi-step interval prediction of uncertainties," *Energy*, vol. 300, p. 131639, 2024.

[25] M. Bai, P. Yao, H. Dong, Z. Fang, W. Jin, Xusheng Yang, J. Liu, and D. Yu, "Spatial-temporal characteristics analysis of solar irradiance forecast errors in europe and north america," *Energy*, vol. 297, p. 131187, 2024.

[26] N. Zhang, C. Kang, Q. Xia, and J. Liang, "Modeling conditional forecast error for wind power in generation scheduling," *IEEE Transactions on Power Systems*, vol. 29, no. 3, pp. 1316–1324, 2014.

[27] C. Chen, C. Liu, L. Ma, T. Chen, Y. Wei, W. Qiu, Z. Lin, and Z. Li, "Cooperative-game-based joint planning and cost allocation for multiple park-level integrated energy systems with shared energy storage," *Journal of Energy Storage*, vol. 73, p. 108861, 2023.

[28] Y. Yang, H. Gao, Y. Xiang, M. Guo, J. Wang, and J. Liu, "Coordinated generation scheduling considering peak regulation cost allocation and compensation distribution in power systems," *Journal of Modern Power Systems and Clean Energy*, vol. 13, no. 6, pp. 1921–1932, 2025.

[29] P. Cao, C. Deng, X. Zhang, Y. Zhang, and Y. Dong, "Real-time coordinated optimal scheduling strategy for thermal power units with adaptive time division and variable objective," *Power System Technology*, vol. 49, pp. 2398–2406, 2025.

[30] J. Wang, S. Zhang, J. Huo, Y. Zhou, L. Li, and T. Han, "Dispatch optimization of thermal power unit flexibility transformation under the deep peak shaving demand based on invasive weed optimization," *Journal of Cleaner*

Production, vol. 315, p. 128047, 2021.

[31] Y. Yun, D. Zhang, L. Li, Y. Li, Y. Shi, and J. He, "Optimal operation strategy of peak regulation combined thermal power units and concentrating solar power plant with energy conversion and spinning reserve," *Journal of Cleaner Production*, vol. 424, p. 138864, 2023.

[32] T. Xie, H. Chang, G. Zhang, K. Zhang, and S. Qing, "Deep power peak regulation of thermal power-energy storage under high proportion of renewable energy access: based on cooperative game method," *Applied Thermal Engineering*, vol. 278, p. 127464, 2025.

[33] J. Li, J. Zhang, G. Mu, Y. Ge, G. Yan, and S. Shi, "Hierarchical optimization scheduling of deep peak shaving for energy-storage auxiliary thermal power generating units," *Power System Technology*, vol. 43, no. 11, pp. 3961–3970, 2019.

[34] N. Q. Minh, N. D. Linh, and N. T. Khiem, "A mixed-integer linear programming model for microgrid optimal scheduling considering bess degradation and res uncertainty," *Journal of Energy Storage*, vol. 104, p. 114663, 2024.

[35] S. Zhang, H. Ye, F. Wang, Y. Chen, S. Rose, and Y. Ma, "Data-aided offline and online screening for security constraint," *IEEE Transactions on Power Systems*, vol. 36, no. 3, pp. 2614–2622, 2021.

[36] H. Ye and Z. Li, "Necessary conditions of line congestions in uncertainty accommodation," *IEEE Transactions on Power Systems*, vol. 31, no. 5, pp. 4165–4166, 2016.